

# Resolving vacuum fluctuations of micromechanical motion using a phonon counter

F. Lecocq, J. D. Teufel, J. Aumentado, R. W. Simmonds

*National Institute of Standards and Technology, 325 Broadway, Boulder, CO 80305, USA*

(Dated: November 11, 2022)

Heisenberg's uncertainty principle results in one of the strangest quantum behaviors: an oscillator can never truly be at rest. Even in its lowest energy state, at a temperature of absolute zero, its position and momentum are still subject to quantum fluctuations. Resolving these fluctuations using linear position measurements is complicated by the fact that classical noise can masquerade as quantum noise. On the other hand, direct energy detection of the oscillator in its ground state makes it appear motionless. So how can we resolve quantum fluctuations? Here, we parametrically couple a micromechanical oscillator to a microwave cavity to prepare the system in its quantum ground state and then amplify the remaining vacuum fluctuations into real energy quanta. Exploiting a superconducting qubit as a photon/phonon number resolving detector we provide the essential non-linear resource to authenticate the unambiguously quantum nature of both light and motion. Our results further demonstrate the ability to control a long-lived mechanical oscillator using a non-Gaussian resource, directly enabling applications in quantum information processing and enhanced detection of displacement and forces.

Quantum mechanics ultimately sets the limits for the simultaneous measurement of two conjugate variables, via Heisenberg's uncertainty principle. This has direct implications on traditional linear measurements and enforces the so-called Standard Quantum Limit (SQL) in both displacement detection and amplification<sup>1</sup>. Cavity optomechanical systems have emerged as an ideal testbed for exploring the quantum limits of linear measurement of macroscopic motion.<sup>2,3</sup> In such systems, a light field reflecting off a mechanical oscillator acquires a position-dependent phase shift and reciprocally, it applies a force onto the mechanical oscillator. This effect is enhanced by embedding the oscillator inside a high-quality factor electromagnetic cavity. Numerous physical implementations exist, both in the microwave and optical domain, and have been used to push the manipulation of macroscopic oscillators into the quantum regime, demonstrating laser cooling to the ground state of motion<sup>4,5</sup>, coherent transfer of itinerant light fields into mechanical motion<sup>6,7</sup> and connecting microwave and optical domains via coherent frequency conversion<sup>8,9</sup>. However, while linear measurements can provide evidence for the quantization of light field via radiation pressure shot noise<sup>10,11</sup> and for mechanical vacuum fluctuations via sideband asymmetry<sup>12</sup>, only careful noise calibrations can rule out a completely classical origin of the effects<sup>13</sup>. Furthermore, the use of only classical signals restricts these experiments to the manipulation of Gaussian states.

These limitations can be overcome using a strongly non-linear element, like a quantum bit (qubit)<sup>14,15</sup>. For example, in the field of circuit-QED, the strong coupling between a microwave cavity and a superconducting qubit has enabled both the preparation and tomography of complex quantum states of light<sup>16-20</sup>. Recently, single phonon control has been demonstrated by coupling a superconducting qubit to a high-frequency mechanical oscillator<sup>21</sup>. Although a pioneering result, short energy life-times of the mechanical oscillator and the qubit have slowed any further progress.

Ideally, one would like to craft a new type of detector that allows both linear and non-linear measurements. Here we do so by combining the advantages of both circuit-QED and microwave optomechanics on a single chip. We present the experimental realization of a non-classical emitter and detector of photons and phonons in an optomechanical system, providing the essential resources to push optomechanics in the quantum realm. Using these tools, we unambiguously reveal the quantum vacuum fluctuations inherently present in both the field of an electro-magnetic cavity and in the motion of a macroscopic oscillator.

A microwave cavity is the central element of this architecture (in blue in Fig.1A). It is a linear inductor-capacitor (LC) resonator formed by a coil inductor and a mechanically compliant vacuum-gap capacitor<sup>22,23</sup>. First, the intra-cavity electromagnetic field is coupled via radiation pressure to the vibrational mode of the compliant capacitor (in red in Fig.1). Second, the microwave cavity is capacitively coupled to a phase qubit (in green in Fig.1). A phase qubit is formed from a Josephson junction in parallel with an LC oscillator, and it behaves like a non-linear resonator at the single quantum level, *i.e.*, an artificial atom<sup>24</sup>. To a good approximation the phase qubit can be operated as a two-level system whose transition frequency  $\omega_{qb}$  can be widely tuned *in situ* by applying an external flux, such that  $9 \text{ GHz} \leq \omega_{qb}/2\pi \leq 13.5 \text{ GHz}$ . The microwave cavity and the fundamental flexural mode of the capacitor are two harmonic oscillators with resonance frequencies of respectively  $\omega_c/2\pi = 10.188 \text{ GHz}$  and  $\Omega_m/2\pi = 15.9 \text{ MHz}$ .

The qubit and the cavity are both electrical circuits with quantized energy levels, sharing a voltage through the coupling capacitor. On resonance,  $\Delta_{qb} = \omega_{qb} - \omega_c = 0$ , the interaction between the qubit and the cavity is well described by the Jaynes-Cummings Hamiltonian  $\mathcal{H}_{jc} = \hbar J (\hat{a}\hat{\sigma}^+ + \hat{a}^\dagger\hat{\sigma}^-)$ .  $\hat{\sigma}^+$  ( $\hat{\sigma}^-$ ) are the raising (lowering) operator for the qubit and  $\hat{a}^\dagger$  ( $\hat{a}$ ) are the creation (annihilation) operators for cavity photons.  $J$  is the ca-

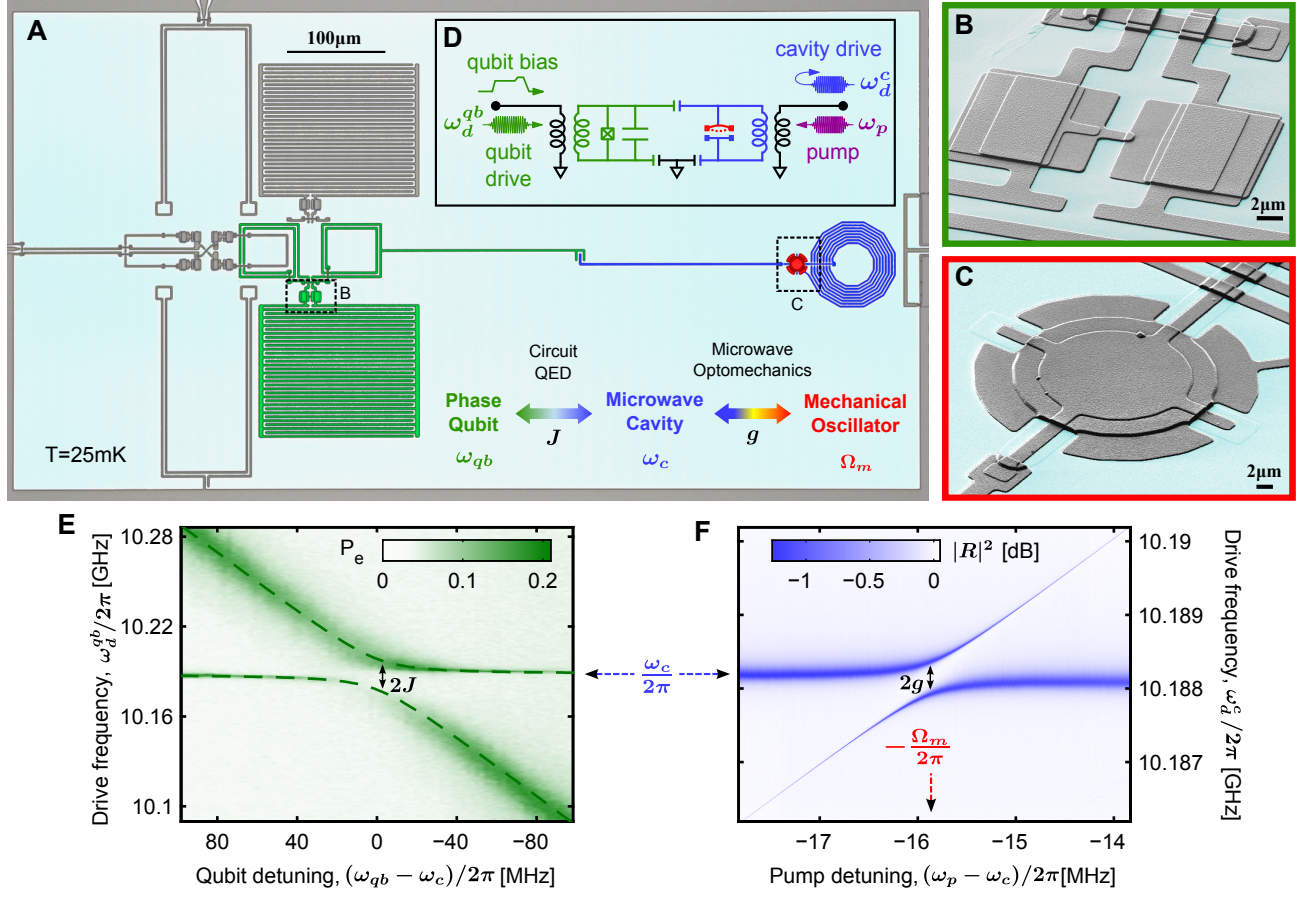


FIG. 1: **Device description and strong coupling regime.** (A), False-color optical micrograph of the device. Aluminum is in grey and sapphire in light blue. The phase qubit is in green; the microwave cavity in blue; and the mechanically compliant capacitor in red. (B,C), False-color scanning electron micrograph of the qubit’s Josephson junction and of the mechanical oscillator, respectively. (D), Equivalent circuit diagram. (E), Qubit/cavity vacuum Rabi splitting. Population of the qubit’s excited state  $P_e$ , in green, as a function of the drive frequency and of the qubit detuning with respect to the microwave cavity. The avoided crossing is a clear signature of the single-photon strong coupling regime. From a fit with theory we extract the qubit/cavity coupling rate  $J = 2\pi \times 12.5$  MHz. (F) Cavity/oscillator normal-mode splitting. Reflected power in blue as a function of the drive and pump frequencies. The drive is applied near the cavity resonance while the pump is applied near  $\Delta_p = -\Omega_m$ . Here, the pump strength is set to  $n_p \approx 5 \times 10^5$ . The normal-mode splitting observed in the cavity driven response corresponds to the hybridization of the cavity and mechanical modes in the driven strong coupling regime. From a fit with theory we extract  $\kappa = 2\pi \times 163$  kHz,  $\Gamma_m = 2\pi \times 150$  Hz and  $g = 2\pi \times 242$  kHz  $> (\bar{n}_m \Gamma_m, \kappa)$  where  $\bar{n}_m \approx 32$  at  $T \approx 25$  mK (see Fig.S2).

capacitive coupling strength.  $\mathcal{H}_{jc}$  describes the exchange of a single quantum between the qubit and the cavity, at a rate  $J$ . In the strong coupling regime, when the coupling strength  $J$  overcomes the decoherence rates of the qubit  $\gamma_{qb}$  and the cavity  $\kappa$ , *i.e.*  $J > (\gamma_{qb}, \kappa)$ , the system hybridizes, leading to the well known vacuum Rabi splitting, measured by spectroscopy in Fig.1E. The qubit-cavity interaction can be effectively turned off by detuning the qubit.

The position of the mechanical oscillator modulates the cavity resonance frequency, thus the energy stored in the cavity. As a result, the microwave photons apply a force on the mechanical oscillator. This interaction is described by the *radiation pressure* Hamiltonian<sup>3</sup>  $\mathcal{H}_{rp} = \hbar G \hat{n}_c \hat{x}$ , where  $G = d\omega_c/dx$ ,  $\hat{n}_c = \hat{a}^\dagger \hat{a}$  is the cav-

ity photon number and  $\hat{x} = x_{zpf} (\hat{b}^\dagger + \hat{b})$  the oscillator’s position. Here,  $x_{zpf}$  is the oscillator’s zero point fluctuation and  $\hat{b}^\dagger$  ( $\hat{b}$ ) is the creation (annihilation) operator for mechanical phonons. The force applied by a single photon onto the mechanical oscillator is typically weak,  $g_0 = G x_{zpf} \ll (\bar{n}_m \Gamma_m, \kappa)$  where  $\bar{n}_m$  is the thermal occupancy of the oscillator and  $\Gamma_m$  its intrinsic relaxation rate<sup>25</sup>. However the total force increases significantly with the intensity of the intra-cavity field. In the presence of a strong coherent microwave pump of frequency  $\omega_p$ , the optomechanical interaction is linearized and takes two different forms depending on the pump-cavity detuning  $\Delta_p = \omega_p - \omega_c$ <sup>25</sup>. When  $\Delta_p = -\Omega_m$ , the annihilation of a mechanical phonon can up-convert a pump photon into a cavity photon, mediating a *beam splitter*

interaction,  $\mathcal{H}_{bs} = \hbar g (\hat{a}\hat{b}^\dagger + \hat{b}\hat{a}^\dagger)$ . This results in the coherent exchange of the cavity and mechanical state at a rate  $g$ , where  $g = g_0\sqrt{\bar{n}_p}$  is the enhanced optomechanical coupling and  $n_p$  is the pump strength expressed in terms of average intra-cavity photons. When  $\Delta_p = +\Omega_m$ , pump photons are parametrically down-converted at a rate  $g$  into correlated pairs of cavity photons and mechanical phonons, inducing parametric amplification and entanglement of the cavity field with the mechanical motion, described by the *two-mode squeezer* Hamiltonian,  $\mathcal{H}_{tms} = \hbar g (\hat{a}^\dagger\hat{b}^\dagger + \hat{b}\hat{a})$ . Once again, the strong coupling regime,  $g > (\Gamma_m, \kappa)$ , is a prerequisite for observing the quantum nature of these two interactions. The hallmark for entering that regime in our device is the hybridization and normal-mode splitting induced by a strong beam splitter interaction<sup>23</sup>, as measured through the cavity driven response in Fig.1F. Finally with a characteristic lifetime of the mechanical oscillator's ground state,  $1/\bar{n}_m\Gamma_m \approx 33 \mu\text{s}$ , much longer than the cavity lifetime,  $1/\kappa \approx 1 \mu\text{s}$ , this device is in the quantum coherent regime<sup>6</sup>.

Measurements in the frequency domain provide an extensive characterization of the device's parameters, however, they only probe the steady state of the system, in equilibrium with the thermal environment. In the following we will show that time domain protocols in the strong coupling regime enable: (1) the preparation of non-classical cavity states and the photon-number measurement of the intra-cavity field<sup>18,19</sup>, and (2) coherent state transfer by frequency conversion and entanglement by parametric amplification between the microwave cavity and the mechanical oscillator<sup>26,27</sup>.

The out-of-equilibrium dynamics between the phase qubit and the cavity are shown in Fig.2. In Fig.2A,B, we initialize the qubit in the excited state using a resonant microwave pulse, then tune the qubit into resonance with the cavity for an interaction time  $\tau$  and monitor the qubit population  $P_e$ . The coupled system undergoes vacuum Rabi oscillations and after half a cycle,  $\tau = \pi/2J$ , the cavity is prepared in a single photon Fock state. Importantly, in addition to the generation of a non-classical state of light, this sequence also provides a calibration of the intra-cavity field amplitude. In Fig.2C-F we initialize the cavity into either a coherent state or a thermal state, of similar average photon occupancy  $\bar{n}_c = \langle \hat{a}^\dagger\hat{a} \rangle$ , and monitor the qubit evolution during the resonant interaction with the cavity. For  $\bar{n}_c < 1$ , the Fock state distributions for a thermal state and a coherent state are very similar and so are the associated qubit evolutions. For  $\bar{n}_c > 1$  both the qubit evolutions and the photon statistics show a marked difference. The evolution of  $P_e(\tau)$  is in very good agreement with simulations where the average photon number  $\bar{n}_c$  is the only free parameter. Note that for  $n_c \geq 10$ , multilevel dynamics of the phase qubit start to induce deviations from the simple two-level model. To summarize, the qubit realizes here a photon-number measurement, calibrated by a single

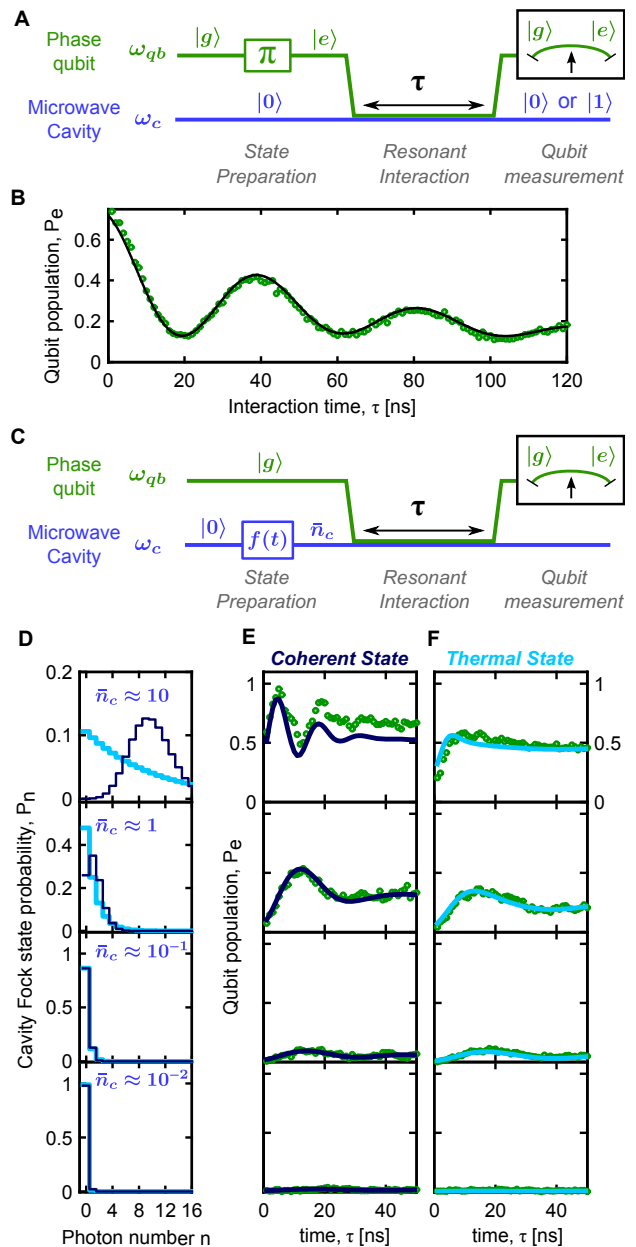


FIG. 2: **Cavity state preparation and readout.** (A), Sequence diagram for the preparation of a single photon Fock state in the cavity. The qubit is prepared in the first excited state  $|e\rangle$  then interacts resonantly with the cavity for a time  $\tau$  before the qubit state is measured. The population of the qubit  $P_e$  is plotted in (B) as a function of the interaction time  $\tau$ . The black line is a fit to a master equation prediction<sup>25</sup>. (C), Sequence diagram for the readout of the cavity state. The cavity is prepared in a coherent (or thermal) state by driving it with a coherent tone (or with white noise). The corresponding intra-cavity photon distributions are shown in (D) for four drive amplitudes, parametrized by the average cavity occupancy  $\bar{n}_c$ . The thermal states distributions and coherent states distributions are respectively in bright and dark blue. For each drive amplitude, the evolution of the qubit population  $P_e$  is plotted in green in (E) for the coherent states, and in (F) for the thermal states. The solid lines are a fit to a master equation prediction<sup>25</sup>.

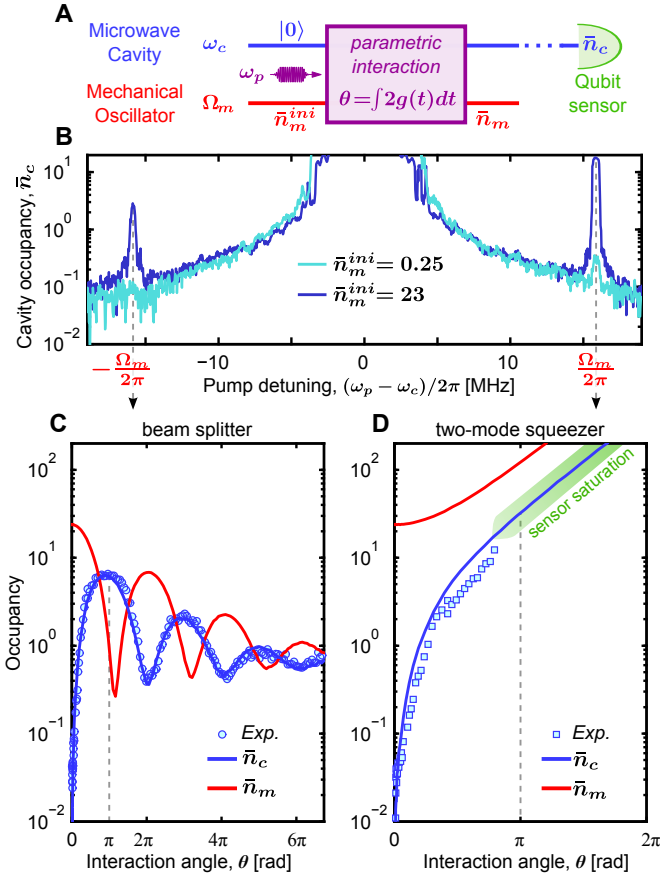


FIG. 3: **Optomechanics with a number resolving detector.** (A) Sequence diagram. (B) Cavity occupancy measured by the qubit as a function of the pump frequency, for a fixed pump duration  $\tau_{pump}$  corresponding to a “ $\pi$  pulse” (here  $n_p = 9 \times 10^4$ ,  $g = 2\pi \times 96$  kHz and  $\tau_{pump} = \pi/2g \approx 2.6$   $\mu$ s). The bright and dark blue curves correspond to an initial oscillator occupancy of  $\bar{n}_m^{ini} = 0.25$  and  $\bar{n}_m^{ini} = 23$ , respectively. (C), Measured cavity occupancy (blue circles) as a function of the interaction duration in reduced unit  $\theta$ , for  $\Delta_p = -\Omega_m$  (here  $n_p = 3.8 \times 10^5$  and  $g = 2\pi \times 198$  kHz). (D), Same as C for  $\Delta_p = +\Omega_m$ . In both C and D the predictions of the Heisenberg-Langevin equations of motion are shown in solid blue<sup>25</sup>. The mechanical occupancy is shown as solid red lines.

photon source, and with a dynamic range ideal for small photon numbers.

A direct measurement of the intra-cavity photon number combined with optomechanical interactions realizes a *phonon*-number measurement. This observable commutes with the oscillator’s Hamiltonian and therefore is not subject to the traditional standard quantum limit associated with linear position measurements<sup>1,3,28</sup>. In the following we exploit that photon/phonon counter to explore the out-of-equilibrium optomechanical dynamics in the strong coupling regime (Fig.3). We start with an active reset where we initialize the average mechanical mode occupancy  $\bar{n}_m^{ini}$  using a strong beam splitter interaction and direct coherent driving of the oscillator,

so that  $\bar{n}_m^{ini} = 23$ . We then apply a large microwave pump for a duration  $\tau_{pump} = \pi/2g$  (corresponding to a “ $\pi$  pulse” when  $\Delta_p = -\Omega_m$  or  $\Delta_p = +\Omega_m$ ). Finally, we tune the qubit into resonance with the cavity to measure the photon distribution of the intra-cavity field, as described previously in Fig.2. The measured occupancy is shown in dark blue in Fig.3B, as a function of the pump-cavity detuning  $\Delta_p$ . It exhibits two clear sidebands at  $\Delta_p = -\Omega_m$  and  $\Delta_p = +\Omega_m$ , corresponding respectively to the transfer of the mechanical state into the cavity or to the amplification of the cavity field via parametric down-conversion. Next, we fix the pump frequency at either  $\Delta_p = -\Omega_m$  (Fig.3C) or  $\Delta_p = +\Omega_m$  (Fig.3D) and vary the pump duration  $\tau_{pump}$ , expressed here in terms of the reduced unit  $\theta \approx 2g\tau_{pump}$ . The measured cavity occupancy, in blue, exhibit two distinct behaviors: when  $\Delta_p = -\Omega_m$  the mechanical state is coherently transferred in and out of the cavity and when  $\Delta_p = +\Omega_m$  the mechanical motion and the cavity field are amplified, resulting eventually in the saturation of the qubit sensor. Data are in very good agreement with numerical simulations, shown as solid blue lines, where the initial mechanical occupancy  $\bar{n}_m^{ini}$  is the only free parameter. The mechanical occupancy,  $\bar{n}_m$ , inferred from these simulations is shown in solid red. The simulations take into account a small but measurable excess cavity noise at high pump power, measured separately<sup>25</sup>. We emphasize that when  $\Delta_p = +\Omega_m$  we monitor the amplification of the two localized modes, ideally generating entanglement<sup>29</sup> at a rate that exceeds the decoherence rates, and when  $\Delta_p = -\Omega_m$  we resolve the coherent exchange of mechanical phonons and cavity photons well below the single quantum level. Notice that a “ $\pi$  pulse” for  $\Delta_p = -\Omega_m$  transfers the cold cavity state into the mechanical oscillator, effectively preparing it close to the ground state, with  $\bar{n}_m = 0.25$ . If we now repeat the measurement in Fig.3B after this ground state initialization, we no longer resolve the lower sideband at  $\Delta_p = -\Omega_m$  because almost no mechanical phonons remain to be transferred into the cavity. On the other hand, we still clearly resolve the cavity amplification at  $\Delta_p = +\Omega_m$ . This is a signature of the asymmetry between the rates of phonon absorption (proportional to  $\bar{n}_m + 1$ ) and emission (proportional to  $\bar{n}_m$ ) when the oscillator is cooled to its ground state<sup>12,30</sup>. This fundamental asymmetry is analogous to the notion of added noise at the quantum limit in the context of three-wave mixing<sup>1,31</sup> and is a consequence of the existence of a half quantum of vacuum fluctuations in these modes.

Our architecture is uniquely suited to explore these regimes in optomechanics because we have the ability to measure directly the mechanically scattered photons, now localized in the cavity. The protocol starts by initializing the mechanical oscillator in a nearly ideal coherent state so that  $\bar{n}_m^{ini} = \bar{n}_m^{th} + |\alpha_m|^2$ , where  $\alpha_m$  is the mechanical displacement and  $\bar{n}_m^{th}$  is the residual thermal phonon occupancy, with  $\bar{n}_m^{th} = 0.25$ . We then apply a microwave pulse with a duration corresponding to a “ $\pi$  pulse”,

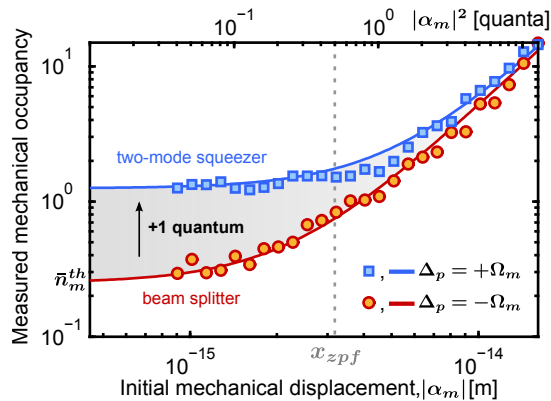


FIG. 4: **Measurement of the vacuum fluctuations.** Initial mechanical occupancy measured from the cavity occupancy after an optomechanical “ $\pi$  pulse” at either  $\Delta_p = -\Omega_m$ , in red, or  $\Delta_p = +\Omega_m$ , in blue, as a function of the initial mechanical displacement. The associated analytical predictions,  $\bar{n}_m^{th} + |\alpha_m|^2$  for  $\Delta_p = -\Omega_m$  and  $\bar{n}_m^{th} + |\alpha_m|^2 + 1$  for  $\Delta_p = +\Omega_m$ , are respectively the red and blue lines.

$\tau_{pump} \approx \pi/2g$ , at either  $\Delta_p = -\Omega_m$  or  $\Delta_p = +\Omega_m$ . Using the qubit we measure the resulting thermal photon occupancy  $\bar{n}_c^{th}$  and displacement  $\alpha_c$  of the cavity state<sup>25</sup>, for a total cavity occupancy  $\bar{n}_c = \bar{n}_c^{th} + |\alpha_c|^2$ . For each process, the cavity displacement allows us to calibrate a gain  $G_{\pm}$  defined as  $\sqrt{G_{\pm}} = |\alpha_c|/|\alpha_m|$ , respectively for  $\Delta_p = \pm\Omega_m$ . The *measured* initial mechanical occupancy is then  $\bar{n}_c/G_{\pm}$ , shown in Fig.4, as a function of the ini-

tial mechanical displacement. For  $\Delta_p = -\Omega_m$ , we measure  $\bar{n}_c/G_{-} = \bar{n}_m^{th}$  whereas for  $\Delta_p = +\Omega_m$ , we measure  $\bar{n}_c/G_{+} = \bar{n}_m^{th} + 1$ . The apparent additional phonon is the inevitable signature of the amplification of the vacuum fluctuations in both modes, to be contrasted with the noiseless character of frequency conversion. The use of a photon/phonon detector leaves no room for a semi-classical description and these results provide clear proof for the quantization of energy and the unavoidable fluctuations of both the mechanical oscillator’s motion and the microwave field.

To conclude, we have built an agile platform for the exquisite control of quantum states in engineered mechanical systems, simultaneously achieving long mechanical lifetime, ground-state cooling, and quantum coherent coupling to a non-classical resource. Looking forward, with more complex protocols we could: (1) exploit the qubit as a deterministic single phonon source to generate arbitrary quantum states of motion, (2) perform full state tomography of the mechanical oscillator and (3) manipulate photon-phonon entanglement via sequenced beam splitter and two-mode squeezer interactions. The ability to encode complex quantum states in these long-lived mechanical systems has important implications for quantum information and for the study of the fundamental quantum behavior of massive objects<sup>32</sup>.

We thank A. W. Sanders for taking the micrographs in Fig.1B,C. This work was supported by the NIST Quantum Information Program. Contribution of the U.S. government, not subject to copyright.

<sup>1</sup> A. A. Clerk, M. H. Devoret, S. M. Girvin, F. Marquardt, R. J. Schoelkopf, *Rev. Mod. Phys.* **82**, 1155 (2010).  
<sup>2</sup> T. J. Kippenberg, K. J. Vahala, *Science* **321**, 1172 (2008).  
<sup>3</sup> M. Aspelmeyer, T. J. Kippenberg, F. Marquardt, *ArXiv e-prints* **1303.0733** (2013).  
<sup>4</sup> J. D. Teufel, *et al.*, *Nature* **475**, 359 (2011).  
<sup>5</sup> J. Chan, *et al.*, *Nature* **478**, 89 (2011).  
<sup>6</sup> E. Verhagen, S. Deleglise, S. Weis, A. Schliesser, T. J. Kippenberg, *Nature* **482**, 63 (2012).  
<sup>7</sup> T. A. Palomaki, J. W. Harlow, J. D. Teufel, R. W. Simmonds, K. W. Lehnert, *Nature* **495**, 210 (2013).  
<sup>8</sup> J. Bochmann, A. Vainsencher, D. D. Awschalom, A. N. Cleland, *Nat. Phys.* **9**, 712 (2013).  
<sup>9</sup> R. W. Andrews, *et al.*, *Nat. Phys.* **10**, 321 (2014).  
<sup>10</sup> T. P. Purdy, R. W. Peterson, C. A. Regal, *Science* **339**, 801 (2013).  
<sup>11</sup> J. Suh, *et al.*, *Science* **344**, 1262 (2014).  
<sup>12</sup> A. H. Safavi-Naeini, *et al.*, *Phys. Rev. Lett.* **108**, 033602 (2012).  
<sup>13</sup> A. H. Safavi-Naeini, *et al.*, *New Journal of Physics* **15**, 035007 (2013).  
<sup>14</sup> S. Haroche, *Rev. Mod. Phys.* **85**, 1083 (2013).  
<sup>15</sup> D. J. Wineland, *Rev. Mod. Phys.* **85**, 1103 (2013).  
<sup>16</sup> A. Wallraff, *et al.*, *Nature* **431**, 162 (2004).

<sup>17</sup> M. A. Sillanpaa, J. I. Park, R. W. Simmonds, *Nature* **449**, 438 (2007).  
<sup>18</sup> M. Hofheinz, *et al.*, *Nature* **454**, 310 (2008).  
<sup>19</sup> M. Hofheinz, *et al.*, *Nature* **459**, 546 (2009).  
<sup>20</sup> G. Kirchmair, *et al.*, *Nature* **495**, 205 (2013).  
<sup>21</sup> A. D. O’Connell, *et al.*, *Nature* **464**, 697 (2010).  
<sup>22</sup> K. Cicak, *et al.*, *Appl. Phys. Lett.* **96**, 093502 (2010).  
<sup>23</sup> J. D. Teufel, *et al.*, *Nature* **471**, 204 (2011).  
<sup>24</sup> R. W. Simmonds, *et al.*, *Phys. Rev. Lett.* **93**, 077003 (2004).  
<sup>25</sup> See *Supplementary Information*.  
<sup>26</sup> E. Zakka-Bajjani, *et al.*, *Nat. Phys.* **7**, 599 (2011).  
<sup>27</sup> S. G. Hofer, W. Wiczorek, M. Aspelmeyer, K. Hammerer, *Phys. Rev. A* **84**, 052327 (2011).  
<sup>28</sup> J. C. Sankey, C. Yang, B. M. Zwickl, A. M. Jayich, J. G. E. Harris, *Nat. Phys.* **6**, 707 (2010).  
<sup>29</sup> T. A. Palomaki, J. D. Teufel, R. W. Simmonds, K. W. Lehnert, *Science* **342**, 710 (2013).  
<sup>30</sup> F. Diedrich, J. C. Bergquist, W. M. Itano, D. J. Wineland, *Phys. Rev. Lett.* **62**, 403 (1989).  
<sup>31</sup> N. Bergeal, *et al.*, *Nat. Phys.* **6**, 296 (2010).  
<sup>32</sup> I. Pikovski, M. R. Vanner, M. Aspelmeyer, M. S. Kim, C. Brukner, *Nat. Phys.* **8**, 393 (2012).

# Supplementary Information for "Resolving vacuum fluctuations of micromechanical motion using a phonon counter"

## Contents

I. Device parameters	2
II. Qubit/Cavity theory	3
III. Optomechanics in the frequency domain	4
IV. Optomechanics in the time domain	4
V. Measurement of the vacuum fluctuations	8
VI. Device fabrication	9
VII. Experimental setup	10
References	13

## I. DEVICE PARAMETERS

A list of the important parameters and notations is presented in the Table S1.

<i>Device parameters</i>		
Phase qubit frequency	$\omega_{qb}$	$9 \text{ GHz} \leq \omega_{qb}/2\pi \leq 13.5 \text{ GHz}$
Microwave cavity frequency	$\omega_c$	$\omega_c/2\pi = 10.188 \text{ GHz}$
Mechanical oscillator frequency	$\Omega_m$	$\Omega_m/2\pi = 15.9 \text{ MHz}$
capacitive coupling strength	$J$	$J = 12.5 \text{ MHz}$
cavity sensitivity	$G$	$G/2\pi = 95 \text{ MHz/nm}$
Mechanical zero-point motion	$x_{zpf}$	$x_{zpf} = 3.18 \text{ fm}$
optomechanical coupling strength	$g_0$	$g_0 = 300 \text{ Hz}$
Mechanical damping rate	$\Gamma_m$	$\Gamma_m/2\pi = 150 \text{ Hz}$
Internal cavity damping rate	$\kappa_{int}$	$150 \text{ kHz} \leq \kappa_{int}/2\pi \leq 1 \text{ MHz}$
External cavity damping rate	$\kappa_{ext}$	$\kappa_{ext}/2\pi = 11 \text{ kHz}$
Single photon cavity decay time	$T_1^{cav}$	$T_1^{cav} = 130 \text{ ns}$
Single photon qubit decay time at 10.5 GHz	$T_1^{qb}$	$T_1^{qb} = 170 \text{ ns}$
Qubit pure dephasing time at 10.2 GHz	$T_\phi^{qb}$	$T_\phi^{qb} = 45 \text{ ns}$

<i>Technical parameters</i>		
Membrane mass	$m$	$m = 52 \text{ pg}$
Membrane radius	$r$	$r = 8.25 \text{ }\mu\text{m}$
Membrane tension	$\sigma$	$\sigma = 320 \text{ MPa}$
Membrane spring constant	$k_s$	$k_s = 530 \text{ N/m}$
Capacitor plate separation	$d$	$d = 40 \text{ nm}$
Membrane capacitance	$C_m$	$C_m = 35 \text{ fF}$
Stray capacitance	$C_s$	$C_s = 13 \text{ fF}$
Cavity coil inductance	$L$	$L = 5 \text{ nH}$
Qubit junction critical current	$I_c^{qb}$	$I_c^{qb} = 0.584 \text{ }\mu\text{A}$
Qubit shunt capacitance	$C_{qb}$	$C_{qb} = 250 \text{ fF}$
Qubit shunt inductance	$L_{qb}$	$L = 1 \text{ nH}$
Qubit/antenna mutual inductance	$M_{antenna/qb}$	$M_{antenna/qb} = 2 \text{ pH}$
SQUID junctions critical current	$I_{1,2,3}^{squid}$	$I_{1,2,3}^{squid} = 1.75, 2.8 \text{ and } 3.15 \text{ }\mu\text{A}$
SQUID inductance	$M_{squid/qb}$	$M = 300 \text{ pH}$
Qubit/SQUID mutual inductance	$M_{squid/qb}$	$M = 70 \text{ pH}$

<i>Combinations and other parameters</i>		
Resolve sideband limit factor	$\Omega_m/\kappa$	$16 \leq \Omega_m/\kappa \leq 88$
Cavity impedance	$Z$	$Z = 380 \text{ }\Omega$
Mechanical quality factor	$Q_m = \Omega_m/\Gamma_m$	$Q_m = 100,000$
Cavity quality factor	$Q_c = \omega_c/\kappa$	$10,000 \leq Q_c \leq 60,000$
Mechanical equilibrium occupancy (T=25mK)	$\bar{n}_m^{bath}$	$\bar{n}_m^{bath} = 32$

<i>Various notations</i>	
Qubit-cavity detuning	$\Delta_{qb} = \omega_{qb} - \omega_c$
Pump-cavity detuning	$\Delta_p = \omega_p - \omega_c$
Cavity occupancy	$n_c = \langle \hat{a}^\dagger \hat{a} \rangle$
Mechanical occupancy	$n_m = \langle \hat{b}^\dagger \hat{b} \rangle$
Initial mechanical occupancy	$\bar{n}_m^i = \langle \hat{b}^\dagger \hat{b} \rangle_{t=0}$
Mechanical thermal occupancy	$n_m^{th}$
Cavity thermal occupancy	$n_c^{th}$
Mechanical displacement	$\alpha_m$
Cavity displacement	$\alpha_c$

TABLE S1: Device parameters and notations

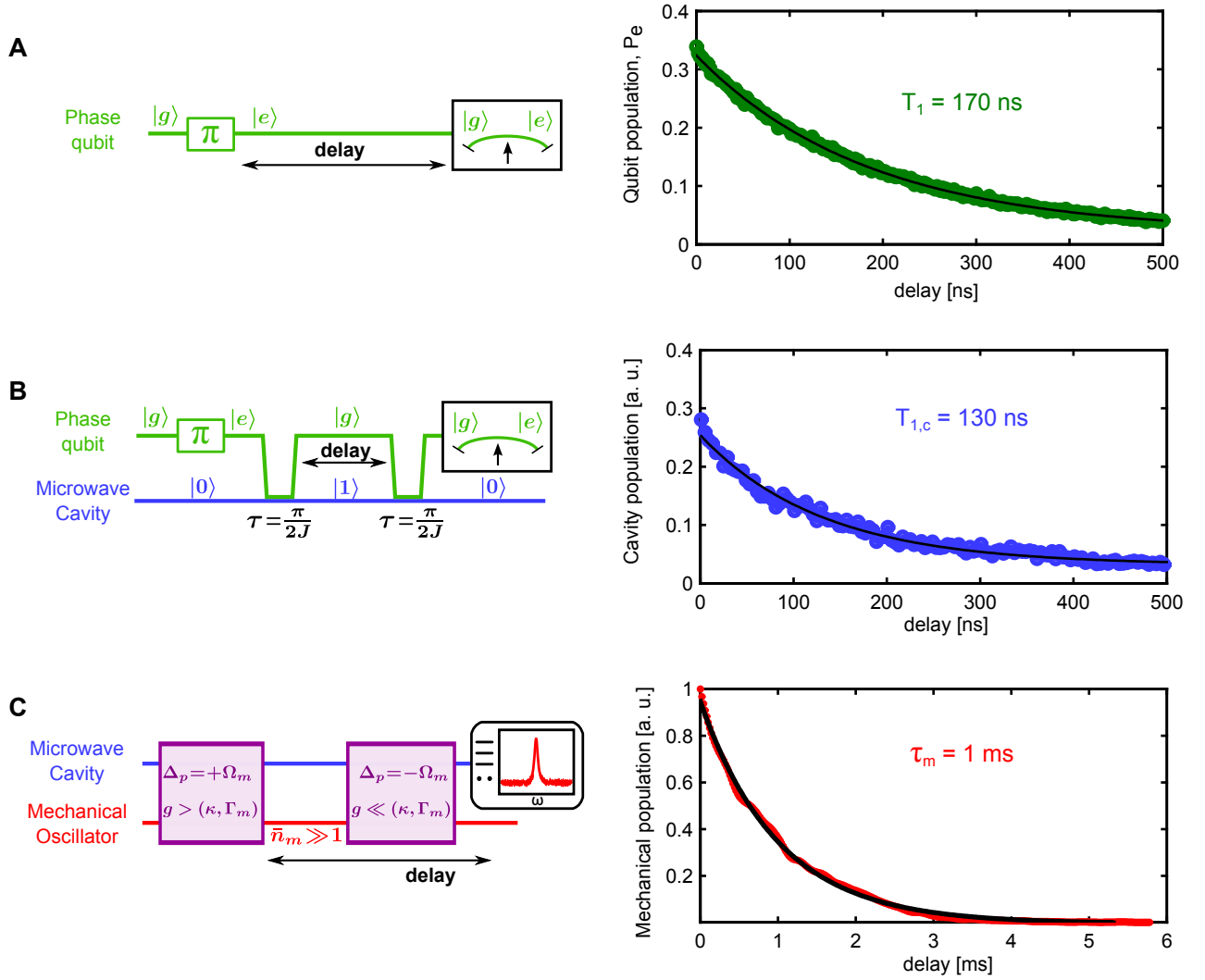


FIG. S1: **Phase qubit, microwave cavity and mechanical oscillator relaxation times.** (A), Qubit relaxation time. (B), Single photon cavity relaxation time measured by storage/retrieval of a single photon Fock state in the cavity. (C), Mechanical “ring-down” time measured by monitoring the decay of the amplitude of the upper sideband of a weak pump tone at  $\Delta_p = \omega_p - \omega_c = -\Omega_m$ , for an initially strongly driven  $\omega$  mechanical oscillator.

## II. QUBIT/CAVITY THEORY

We develop here the theoretical framework for the qubit/cavity interaction, leading to the use of the qubit as a single photon source and a photon-number resolving detector. The Hamiltonian describing the coupled system qubit/cavity alone is:

$$\mathcal{H}_{qed}(t) = \frac{1}{2}\hbar\omega_{qb}(t)\hat{\sigma}_Z + \hbar\omega_c \left( \hat{a}^\dagger \hat{a} + \frac{1}{2} \right) + \hbar J (\hat{a}\hat{\sigma}_+ + \hat{a}^\dagger\hat{\sigma}_-) \quad (1)$$

The out-of-equilibrium quantum dynamics in the presence of relaxation and decoherence is captured by the following Lindblad master equation<sup>1</sup>:

$$\dot{\rho}(t) = -\frac{i}{\hbar} [\mathcal{H}_{qed}(t), \rho(t)] + \frac{1}{2} \sum_n [C_n, \rho(t)C_n^\dagger] + [C_n\rho(t), C_n^\dagger] \quad (2)$$

where  $C_n$  are operators describing: qubit relaxation  $C_1 = \sqrt{1/T_1}\hat{\sigma}^-$ ; cavity relaxation  $C_2 = \sqrt{1/T_{1,cav}}\hat{a}$ ; and qubit pure dephasing  $C_3 = \sqrt{2/T_\phi}\hat{\sigma}_z$ .

To fit the qubit population oscillation in Fig.2A, we numerically integrate Eq.2 (using QuTiP<sup>2</sup>). We introduce the full time dependence of  $\omega_{qb}(t)$  into  $\mathcal{H}_{qed}(t)$ , including the 4 ns risetime of the pulse that tunes the qubit into resonance with the cavity, as well as a small linear drift of the qubit frequency during the interaction. We also account for excited state preparation fidelity of about 75% and a measurement contrast of 51%, which agrees with the total visibility of 35% measured with the qubit relaxation measurement of Fig.S1A. We use  $T_1 = 160$  ns,  $T_{1,cav} = 110$  ns and  $T_\phi = 45$  ns, in very good agreement with the independent measurements of Fig.S1A,B.

The fit of the single photon vacuum Rabi oscillations also provides a full calibration of the qubit sensor. The fitting procedure of the qubit evolution used in Fig.2B, Fig.3 and Fig.4 can now be strongly constrained to only two parameters: the cavity photon distribution and an eventual qubit flux offset (that impacts the qubit/cavity detuning and the contrast of the qubit state measurement). In Fig.2B the distribution is chosen to be either Poissonian or thermal and the average photon number is the fit parameter. In Fig.3 and Fig.4 we more generally consider a displaced thermal state.

### III. OPTOMECHANICS IN THE FREQUENCY DOMAIN

The microwave cavity's driven response is dressed by its interaction with the mechanical oscillator and gives access to most of the parameters of the system<sup>3</sup>. The reflected signal off of the cavity in the presence of a microwave pump, as presented in Fig.1F, follows<sup>4,5</sup>:

$$R = \frac{1}{1 + i\alpha_f} - \frac{2\eta\kappa(1 - i\chi)}{\kappa + 2i(\omega - \omega_c) + 4\chi(\omega_p - \omega_c)} \quad (3)$$

with

$$\chi = \frac{4g^2\Omega_m}{(\kappa + 2i(\omega - 2\omega_p + \omega_c))(\Omega_m^2 - (\omega - \omega_p)^2 + i(\omega - \omega_p)\Gamma_m)} \quad (4)$$

In the above  $\omega_c$  is the microwave cavity frequency;  $\Omega_m$  is the mechanical oscillator frequency;  $\omega_p$  is the pump frequency;  $\Gamma_m$  is the intrinsic mechanical linewidth;  $\kappa = \kappa_{int} + \kappa_{ext}$  is the total cavity linewidth, where  $\kappa_{ext}$  is the decay rate to the feed line and  $\kappa_{int}$  is the decay rate to the environment;  $\eta = \kappa_{ext}/\kappa$  is the coupling parameter;  $\alpha_f$  is the fano parameter;  $g = Gx_{zpf}\sqrt{n_p}$  is the enhanced optomechanical coupling; and  $n_p$  is the pump strength expressed in photon units:

$$n_p = \frac{4P_{in}\kappa_{ext}}{\hbar\omega_p(\kappa^2 + 4(\omega_p - \omega_c)^2)} \quad (5)$$

where  $P_{in}$  is the incident microwave power.

Three individual spectra from Fig.1F and the associated fits to Eq.3 are presented in Fig.S2, for a fixed pump strength  $n_p = 447 \times 10^3$ , showing very good agreement between theory and experiment.

A fit to the cavity driven response for  $\Delta_p = -\Omega_m$  as a function of power allows us to extract the optomechanical coupling  $g$  as a function of the pump strength  $n_p$ , in purple in Fig.S2D. Our data follow the expected  $g = g_0\sqrt{n_p}$  behaviour and we extract  $g_0 = 300$  Hz. Also, in orange, we plot the optomechanical coupling strength obtained from the swap rate between the microwave cavity and the mechanical oscillator, measured following the same sequence as in Fig.3 and Fig.S3.

### IV. OPTOMECHANICS IN THE TIME DOMAIN

In this section we introduce the theory that describes the out-of-equilibrium dynamics of the optomechanical system. Similar derivations can be found in other references<sup>6-10</sup>. The main goal here is to write the Equations of Motion (EoM) of the system. We will then numerically integrate these EoM and compare the predictions to our data. In the following, the qubit is far detuned from the cavity (up to  $\Delta_{qb} \approx 2\pi \times 3.5$  GHz  $\approx 280 \times J$ ) and we can neglect its interaction.

We start with the Hamiltonian describing the coupled cavity/oscillator system:

$$\hat{\mathcal{H}}_{om} = \hbar\omega_c\hat{a}^\dagger\hat{a} + \hbar\Omega_m\hat{b}^\dagger\hat{b} + \hat{\mathcal{H}}_{rp} \quad (6)$$

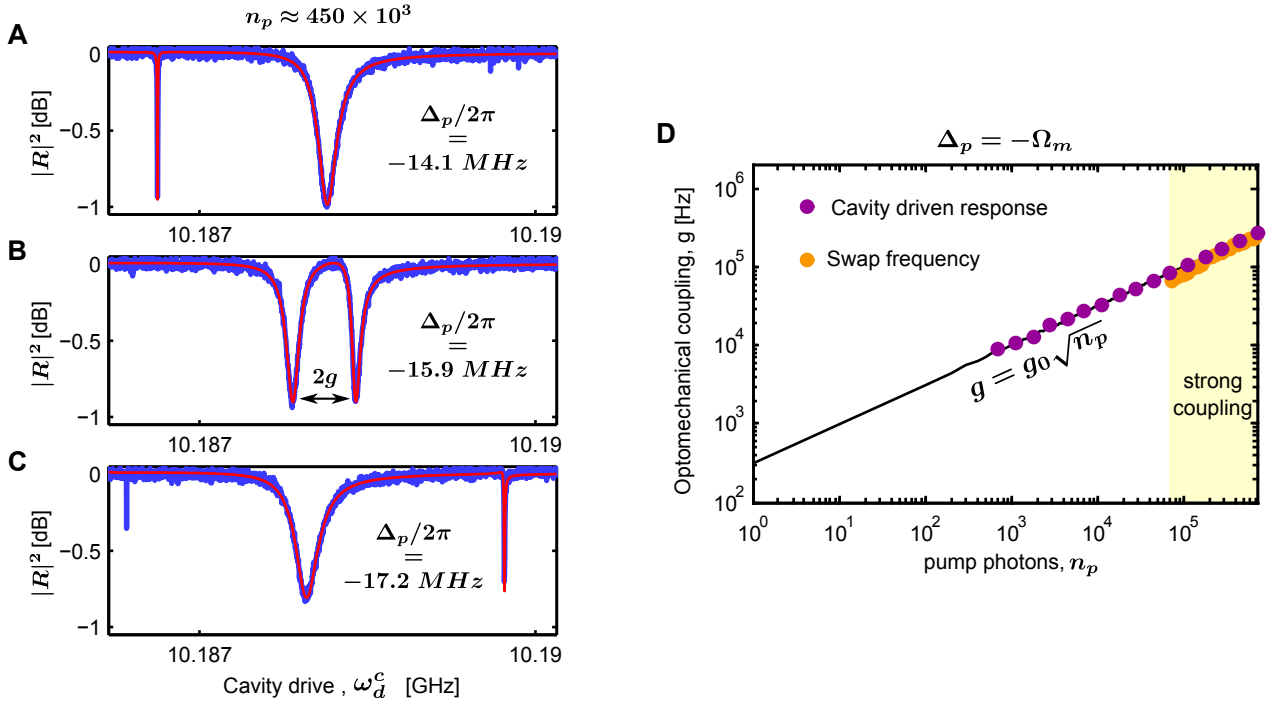


FIG. S2: **Cavity driven response and optomechanical coupling.** (A), (B), (C), Driven response measured in presence of a strong pump for three different detuning and a fixed pump power so that  $n_p = 447 \times 10^3$ . The fit to Eq.3 is shown in red. (D), coupling rate as a function of  $n_p$ . The purple points are measured from the cavity driven response when  $\Delta_p = -\Omega_m$ , like in (B). The orange points are measured from the swap rate between the mechanical oscillator and the microwave cavity, using the same sequence than in Fig.3 and Fig.S3.

where  $\hat{\mathcal{H}}_{rp}$  describes the work done by the microwave radiation force onto the mechanical motion:

$$\hat{\mathcal{H}}_{rp} = \hbar g_0 \hat{a}^\dagger \hat{a} (\hat{b}^\dagger + \hat{b}) \quad (7)$$

The Heisenberg-Langevin EoM using input-output formalism are<sup>6</sup>:

$$\dot{\hat{a}}(t) = -\frac{i}{\hbar} [\hat{a}, \hat{\mathcal{H}}_{om}] - \frac{\kappa}{2} \hat{a} + \sqrt{\kappa_{ext}} \hat{\xi}_{ext} + \sqrt{\kappa_{int}} \hat{\xi}_{int} \quad (8)$$

$$\dot{\hat{b}}(t) = -\frac{i}{\hbar} [\hat{b}, \hat{\mathcal{H}}_{om}] - \frac{\Gamma_m}{2} \hat{b} + \sqrt{\Gamma_m} \hat{\xi}_m \quad (9)$$

which includes the input noise operators associated with the different baths of the system: the external control line of the cavity  $\hat{\xi}_{ext}$ , the internal bath of the cavity  $\hat{\xi}_{int}$  and the internal bath of the oscillator  $\hat{\xi}_m$ .

To capture the dynamics of the coupled modes amplitudes in presence of a strong classical microwave pump, we proceed to the transformation:

$$\hat{a} \rightarrow \alpha e^{i\omega_p t} + \hat{a} e^{i\omega_c t} \quad (10)$$

$$\hat{b} \rightarrow b_0 + \hat{b} e^{i\Omega_m t} \quad (11)$$

where  $\omega_p$  and  $\alpha$  are the frequency and amplitude of the pump;  $b_0$  is the steady state mechanical position in presence of the pump and  $\hat{a}$  and  $\hat{b}$  describe now the fluctuation around the steady state at the cavity frequency and mechanical frequency, respectively. Note that  $\omega_c$  is renormalized to  $\omega_c \rightarrow \omega_c + g_0(b_0 + b_0^*)$ , without a change of notation, for clarity. We will assume  $\alpha$  is real and  $\alpha = |\sqrt{n_p}| \gg 1$ . We can now linearize the Hamiltonian  $\hat{\mathcal{H}}_{rp}$  by expanding in powers of  $\alpha$ , keeping the terms of orders  $|\alpha|^1$ . Although relatively complex in general the interaction Hamiltonian can take very simple forms for the following specific cases.

Case 1: when  $\Delta_p = \omega_p - \omega_c = -\Omega_m$ , we get under the rotating wave approximation

$$\hat{\mathcal{H}}_{rp} \approx \hat{\mathcal{H}}_{bs} = \hbar g (\hat{a}\hat{b}^\dagger + \hat{b}\hat{a}^\dagger). \quad (12)$$

Case 2: when  $\Delta_p = \omega_p - \omega_c = +\Omega_m$ , we get under the rotating wave approximation

$$\hat{\mathcal{H}}_{rp} \approx \hat{\mathcal{H}}_{tms} = \hbar g (\hat{a}^\dagger\hat{b}^\dagger + \hat{b}\hat{a}). \quad (13)$$

Here  $g = g_0\alpha$  is the parametrically enhanced optomechanical coupling. These simplifications of  $\hat{\mathcal{H}}_{rp}$  can be understood from a simple energy conservation argument. When  $\omega_p = \omega_c + \Omega_m$  only the parametric down conversion of pump photons into cavity photons and mechanical phonons conserves energy ( $\hat{\mathcal{H}}_{tms}$ ). When  $\omega_p = \omega_c - \Omega_m$  the pump mediates the exchange interaction, also known as beam splitter  $\hat{\mathcal{H}}_{bs}$ , by the allowing the combination of mechanical phonons and pump photons to generate cavity photons.

To capture the dynamics in the presence of pulsed optomechanical interactions, we now consider a time-dependent number of pump photons  $n_r(t)$  and  $n_b(t)$ , respectively at the pump frequencies  $\Delta_p = -\Omega_m$  and  $\Delta_p = +\Omega_m$ , leading to two different coupling rates  $g_{r,b}(t) = g_0|\sqrt{n_{r,b}(t)}|$ . The coupled EoM, Eq.8 and Eq.9, becomes:

$$\frac{d}{dt} \begin{bmatrix} \hat{a} \\ \hat{b} \\ \hat{a}^\dagger \\ \hat{b}^\dagger \end{bmatrix} = \begin{bmatrix} -\kappa/2 & ig_r(t) & 0 & ig_b(t) \\ ig_r(t) & -\Gamma_m/2 & ig_b(t) & 0 \\ 0 & -ig_b(t) & -\kappa/2 & -ig_r(t) \\ -ig_b(t) & 0 & -ig_r(t) & -\Gamma_m/2 \end{bmatrix} \begin{bmatrix} \hat{a} \\ \hat{b} \\ \hat{a}^\dagger \\ \hat{b}^\dagger \end{bmatrix} + \begin{bmatrix} \sqrt{\kappa_{ext}} & \sqrt{\kappa_{int}} & 0 & 0 & 0 & 0 \\ 0 & 0 & \sqrt{\Gamma_m} & 0 & 0 & 0 \\ 0 & 0 & 0 & \sqrt{\kappa_{ext}} & \sqrt{\kappa_{int}} & 0 \\ 0 & 0 & 0 & 0 & 0 & \Gamma_m \end{bmatrix} \begin{bmatrix} \hat{\xi}_{ext} \\ \hat{\xi}_{int} \\ \hat{\xi}_m \\ \hat{\xi}_{ext}^\dagger \\ \hat{\xi}_{int}^\dagger \\ \hat{\xi}_m^\dagger \end{bmatrix} \quad (14)$$

We can write these equations in the quadrature basis  $\{\hat{X}_c, \hat{X}_m, \hat{Y}_c, \hat{Y}_m\}$  following the transformation:

$$\begin{bmatrix} \hat{X}_c \\ \hat{X}_m \\ \hat{Y}_c \\ \hat{Y}_m \end{bmatrix} = \frac{1}{2} \begin{bmatrix} 1 & 0 & 1 & 0 \\ 0 & 1 & 0 & 1 \\ -i & 0 & i & 0 \\ 0 & -i & 0 & i \end{bmatrix} \begin{bmatrix} \hat{a} \\ \hat{b} \\ \hat{a}^\dagger \\ \hat{b}^\dagger \end{bmatrix} \quad (15)$$

In this basis the thermal occupancy of the cavity mode and mechanical mode,  $n_{c,m}^{th}$ , and their displacement amplitude  $\alpha_{c,m}$ , are:

$$|\alpha_{c,m}|^2 = \langle \hat{X}_{c,m} \rangle^2 + \langle \hat{Y}_{c,m} \rangle^2 \quad (16)$$

$$n_{c,m}^{th} = \langle \hat{X}_{c,m}^2 \rangle + \langle \hat{Y}_{c,m}^2 \rangle - \frac{1}{2} - |\alpha_{c,m}|^2 \quad (17)$$

We can now numerically integrate Eq.14 to predict the behaviour of  $n_{c,m}^{th}$  and  $\alpha_{c,m}$ . The circuit parameters are known from the measurements in the frequency domain described in the previous section. The noise operators correspond to white noise and follow  $\langle \hat{\xi}_{ext,int,m}^\dagger(t)\hat{\xi}_{ext,int,m}(0) \rangle = \bar{n}_{ext,int,m}^{bath}\delta(t)$ . Here:  $\bar{n}_m^{bath}$  is the equilibrium Bose-Einstein occupancy  $\bar{n}_m^{bath} = [\exp(\hbar\Omega_m/k_bT) - 1]^{-1} \approx 32$  for  $T = 25$  mK;  $\bar{n}_{ext}^{bath} = 0$ ; and, although the environment temperature for the microwave cavity mode,  $\bar{n}_{int}^{bath}$ , should be negligible it appears to be finite and dependent on the pump strength, as measured independently in Fig.S4 (discussed further in that section). The only remaining free parameters are the initial mechanical thermal occupancy and its displacement:  $\bar{n}_m^{ini} = \bar{n}_m^{th} + |\alpha_m|^2$ . We finally repeat the integration of Eq.14 for  $10^4$  initial input states configuration, with a Gaussian distribution of known variance, and extract the moments of the output distribution to estimate  $n_{c,m}^{th}$  and  $\alpha_{c,m}$ .

In Fig.S3 we compare the predictions of the EoM with our data, for four different pump powers and two initial mechanical states, as a function of the interaction duration  $\tau_{pump}$ , expressed in reduced unit  $\theta = \int 2g_{r,b}(t)dt$ . Note that Fig.S3C is similar to Fig.3B in the main text. Here we display the *measured* occupancy  $\bar{n}$  in green and the theoretical predictions in black. The *predicted* cavity occupancy  $\bar{n}_c$  and mechanical occupancy  $\bar{n}_m$ , just after the

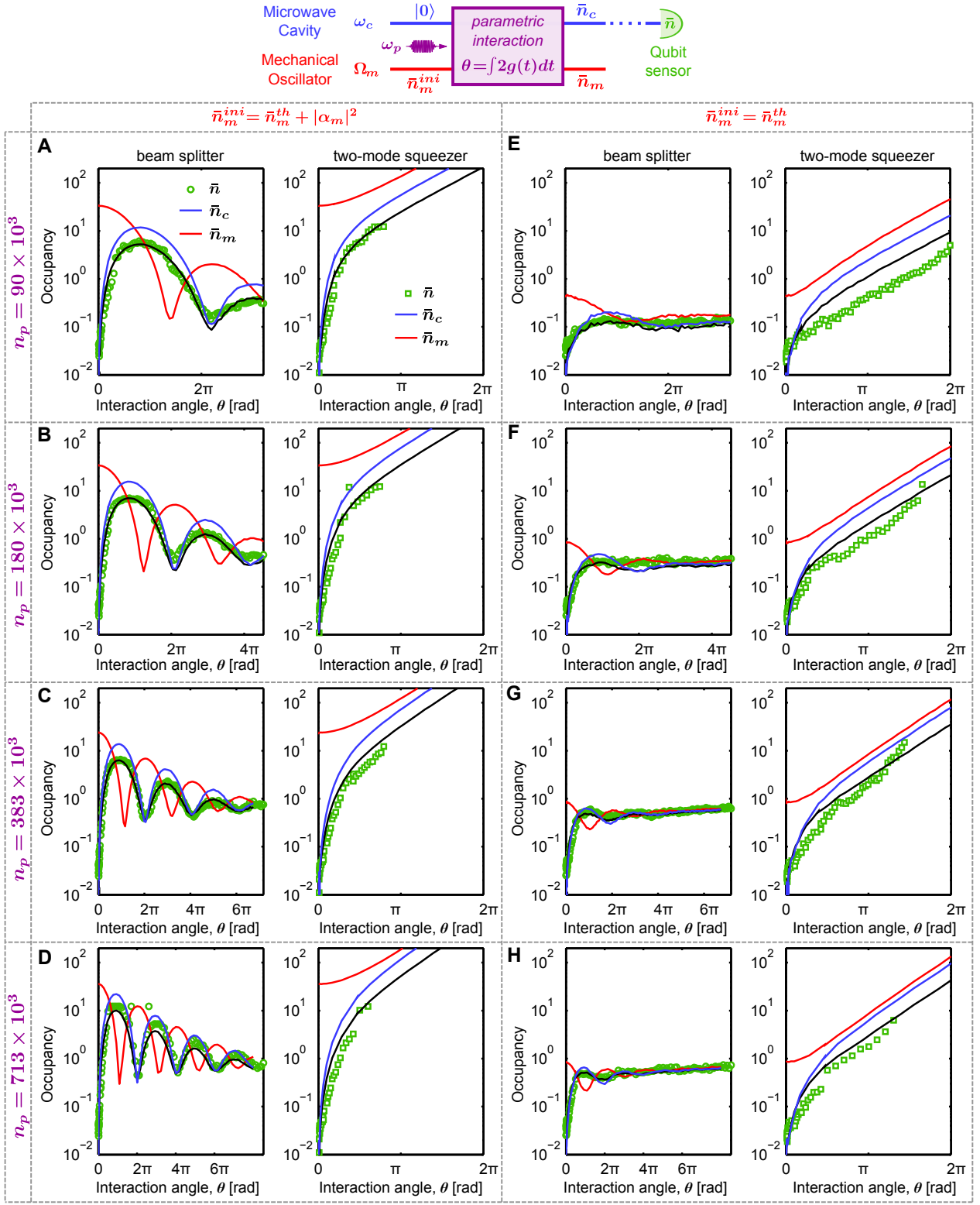


FIG. S3: **Pulsed optomechanics with a qubit readout.** Measured cavity occupancy, in green, as a function of interaction duration in reduced units  $\theta$ , for  $\Delta_p = -\Omega_m$  and  $\Delta_p = +\Omega_m$ . Comparison with prediction from Eq.14 is shown in black, with the initial mechanical state as a fit parameter. Inferred cavity and mechanical occupancy, just after the optomechanical interaction, are shown respectively in blue and red. From (A) to (D) and from (E) to (H) the pump amplitude increases from  $n_p = 90 \times 10^3$  to  $n_p = 713 \times 10^3$ . In all cases the mechanical mode is initially precooled down to  $\bar{n}_m^{ini} = \bar{n}_m^{th}$  and in A, B, C, D it is driven up to  $\bar{n}_m^{ini} = \bar{n}_m^{th} + |\alpha_m|^2$ . (C) displays the same data than Fig.3C, with a slightly different color coding that emphasizes the difference between *measured* and *inferred* cavity occupancy (Methods).

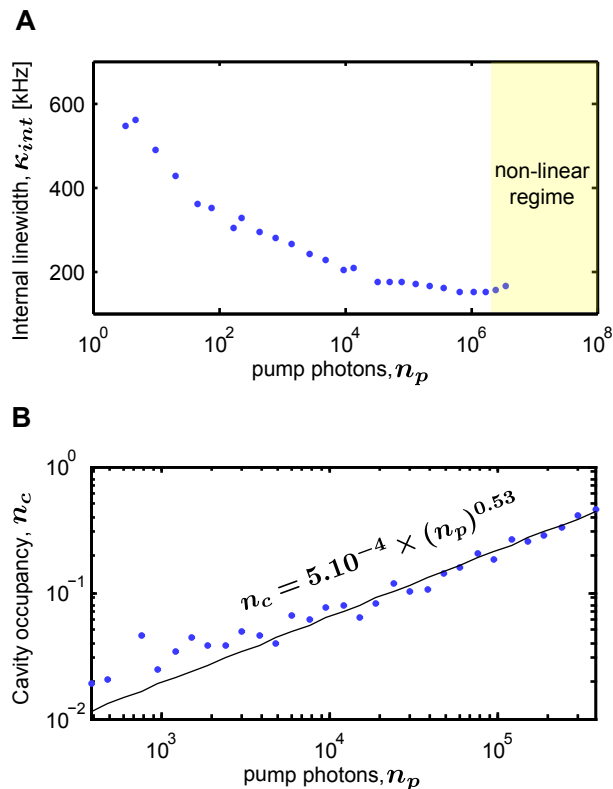


FIG. S4: **Signatures of dielectric loss in the microwave cavity.** (A), Internal cavity loss as a function of the probe tone strength, expressed in units of intra-cavity photons (see Eq.5). (B), Excess cavity occupancy measured after a  $\approx 10 \mu\text{s}$  pulse at  $\Delta_p = -\Omega_m$  with the mechanical mode pre-cooled to  $\bar{n}_m^{ini} < 1$ , as a function of pump power. It corresponds to the population measured at the highest interaction angle in Fig.S3E, F, G and H.

optomechanical interaction, are shown respectively in blue and red. The difference between the cavity occupancy as measured by the qubit sensor,  $\bar{n}$ , and the expected cavity occupancy at the end of the optomechanical interaction,  $\bar{n}_c$ , comes simply from the cavity relaxation during the delay between the end of the optomechanical interaction and the qubit/cavity resonant interaction. The distinction between  $\bar{n}$  and  $\bar{n}_c$  is not made in the main text, for clarity. Overall, the predictions are in excellent agreement with the data, exhibiting a well understood scaling of the exchange rate between the cavity and the oscillator for  $\Delta_p = -\Omega_m$  and of the amplification rate for  $\Delta_p = +\Omega_m$ .

One of the recurrent features we observe when measuring the cavity population evolution for  $\Delta_p = -\Omega_m$  is that even though the microwave cavity starts cold (initial occupancy  $\bar{n}_c^{ini} \approx 10^{-2}$ ) it is driven by excess noise during the interaction, forcing the two modes to equilibrate at a much higher occupancy. The excess noise increases with the pump power, as shown in Fig.S4A where we measure the final equilibrium occupancy of the cavity  $\bar{n}_c = \bar{n}_{int}^{bath}$  for various pump power. At the highest pump powers the occupancy of the cavity reaches a few tens of quanta.

To explain this excess noise we start by ruling out simple origins like phase or amplitude noise of the pump (linear with power and already filtered out, as shown in Fig.S8). To rule out Joule heating at the feedline port's load we note that the cavity is strongly under-coupled,  $\eta = \kappa_{ext}/\kappa_{int} < 10\%$ , which implies that the feedline port would have to have a temperature of  $T_{ext} = T_{cav}/\eta > 4 \text{ K}$ , unrealistic experimentally. We also rule out Joule heating of the substrate since the qubit would also be affected, but this is not observed. Finally, we converge toward a hot bath of spurious TLSs in the surface dielectrics<sup>11,12</sup>, consistent with the observed power law in Fig.S4A and the power dependent internal quality factor of the cavity shown in Fig.S4B.

## V. MEASUREMENT OF THE VACUUM FLUCTUATIONS

In this section we will describe the theory, assumptions and the experimental details related to the measurement of the vacuum fluctuations of the mechanical oscillator's motion and the microwave field, shown in Fig.4.

To provide more intuition let's start from an ideal, lossless, case:  $\kappa_{int} = \kappa_{ext} = \Gamma_m = 0$ . Eq.14 becomes simply:

$$\frac{d}{dt} \begin{bmatrix} \hat{a} \\ \hat{b} \\ \hat{a}^\dagger \\ \hat{b}^\dagger \end{bmatrix} = \begin{bmatrix} 0 & -ig_r & 0 & -ig_b \\ -ig_r & 0 & -ig_b & 0 \\ 0 & ig_b & 0 & ig_r \\ ig_b & 0 & ig_r & 0 \end{bmatrix} \begin{bmatrix} \hat{a} \\ \hat{b} \\ \hat{a}^\dagger \\ \hat{b}^\dagger \end{bmatrix} \quad (18)$$

These coupled modes equations are easily solved analytically to extract the evolution of  $\bar{n}_c = \langle \hat{a}^\dagger \hat{a} \rangle$  for a given initial mechanical state  $\bar{n}_m^{ini}$  and cavity state  $\bar{n}_c^{ini}$ .

For a beam splitter ( $\Delta_p = -\Omega_m$  and  $g_b = 0$ ), and defining  $\theta_r = 2g_r t$ , one gets:

$$\bar{n}_c^{bs} + \frac{1}{2} = \left( \bar{n}_c^{ini} + \frac{1}{2} \right) \cos^2 \left( \frac{\theta_r}{2} \right) + \left( \bar{n}_m^{ini} + \frac{1}{2} \right) \sin^2 \left( \frac{\theta_r}{2} \right) \quad (19)$$

For the two-mode squeezer ( $\Delta_p = +\Omega_m$  and  $g_r = 0$ ), and defining  $\theta_b = 2g_b t$ , one gets:

$$\bar{n}_c^{tms} + \frac{1}{2} = \left( \bar{n}_c^{ini} + \frac{1}{2} \right) ch^2 \left( \frac{\theta_b}{2} \right) + \left( \bar{n}_m^{ini} + \frac{1}{2} \right) sh^2 \left( \frac{\theta_b}{2} \right) \quad (20)$$

Basic trigonometric identities greatly simplifies Eq.19 and Eq.20 when considering a cavity starting in the ground state,  $\bar{n}_c^{ini} = 0$ , and referring the output cavity state back to the mechanical input state:

$$\frac{\bar{n}_c^{bs}}{\sin^2(\theta_r/2)} = \bar{n}_m^{ini} \quad (21)$$

$$\frac{\bar{n}_c^{tms}}{sh^2(\theta_b/2)} = \bar{n}_m^{ini} + 1 \quad (22)$$

An added quanta is revealed in Eq.22, arising from the amplification of the half-quantum of vacuum fluctuations in each modes.

We now include losses and coupling to the different baths in the system. Losses reduce the efficiency for each processes and are easily measured by preparing a displaced initial mechanical state. We define  $G_-$  and  $G_+$  from the ratio of the initial mechanical displacement  $|\alpha_m|$  and the final cavity displacement  $|\alpha_c|$ , so that  $\sqrt{G_\pm} = |\alpha_c|/|\alpha_m|$ , respectively for  $\Delta_p = \pm\Omega_m$ . Equations 21 and 22 become:

$$\frac{\bar{n}_c^{bs}}{G_-} = \bar{n}_m^{ini} \quad (23)$$

$$\frac{\bar{n}_c^{tms}}{G_+} = \bar{n}_m^{ini} + 1 \quad (24)$$

The finite mechanical bath temperature can be neglected because the timescales associated with the mechanical oscillator are small to first order,  $\Gamma_m, \Gamma_{th} \ll g, \kappa, \kappa_{th}$ , where  $\kappa_{th} = \bar{n}_{int}^{bath} \kappa$ . To account for the finite cavity bath temperature discussed previously, we assume that the small cavity occupancy driven by the excess noise adds up linearly to the total cavity occupancy and do not participate directly in the optomechanical interaction (not being transferred by  $\hat{\mathcal{H}}_{bs}$ , nor amplified by  $\hat{\mathcal{H}}_{tms}$ ). This approximation shows very good agreement with simulation for  $g > \kappa_{th}$ , and in particular for our parameters  $g/\kappa_{th} \approx 3$ . For either the beam splitter or the two-mode squeezer the contribution of the optomechanical interaction is retrieved from the measured cavity occupancy following:

$$\bar{n}_c = \bar{n}_c^{bs,tms} + \bar{n}_{int}^{bath} (1 - e^{-\kappa_{opt} t}) \quad (25)$$

Where  $\bar{n}_{int}^{bath}$  is the bath occupancy extracted in Fig.S4A,  $\kappa_{opt}$  is the effective cavity linewidth during the optomechanical interaction ( $\kappa_{opt} \approx \kappa/2$  when  $\Delta_p = -\Omega_m$  and  $\kappa_{opt} \approx \kappa$  when  $\Delta_p = +\Omega_m$ ).

Data shown in Fig.S5 are measured following the same sequence than in Fig.S3, for a fixed interaction angle  $\theta = \pi$ , a fixed pump amplitude  $n_d = 383 \times 10^3$  and for a wide range of displacements,  $\alpha_m$ . In previous measurements we have extracted all the loss rates, interaction strengths and cavity thermal occupancy arising from the finite bath temperature. We can therefore infer the cavity state resulting from the optomechanical interactions alone and observe a very good agreement with Eq.23 and Eq.24, shown in Fig.4 in the main text.

## VI. DEVICE FABRICATION

The device was fabricated on a sapphire substrate using standard optical lithography techniques. The process is illustrated and outlined in Fig.S6.

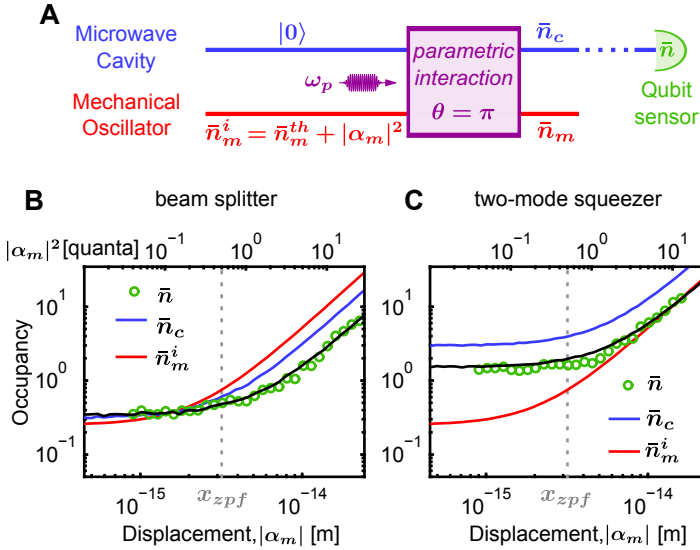


FIG. S5: **Sideband asymmetry.** (A) Pulse sequence. (B,C) Measured occupancy, in green, as a function of initial mechanical displacement  $\alpha_m$ , for  $\Delta_p = -\Omega_m$  and  $\Delta_p = +\Omega_m$ . Comparison with prediction from Eq.14 is shown in black, with the initial mechanical state as a fit parameter. The cavity occupancy *just after the optomechanical interaction* is shown in blue. The *initial* mechanical occupancy is shown in red.

## VII. EXPERIMENTAL SETUP

The chip is wire-bonded to a microwave circuit board, encased in a brass sample box and then anchored to the mixing chamber stage of a dilution refrigerator ( $T \approx 25$  mK). To protect the circuit from stray magnetic fields we shield the sample box with two concentric Cryoperm cylinders. The dewar itself is also protected by a mu-metal shield. All the signals are routed down to the device, from room temperature, via coaxial cables. We will describe in the following the signal generation and measurement for the different components of the device. The full experimental setup is shown in Fig.S7.

*Microwave optomechanics* For the control and measurement of the optomechanical device, a total of four different microwave tones are sent down the fridge via one single coaxial line, attenuated at each temperature stage. The microwave pump (used to produce the parametric coupling between the cavity and the mechanical oscillator) creates the most stringent requirements. The pump strength required to enter the strong optomechanical coupling regime correspond to a large number of intra-cavity photon  $n_p > 10^5$  at  $\Delta_p = \pm\Omega_m$ . That pump is generated and pulsed at room temperature using a high power vector signal generator with integrated IQ mixers driven by an Arbitrary Waveform Generator (AWG). This allows for a maximum output power of 25 dBm *after the mixer*. Here is a list of the requirements:

- To maintain a negligible intra-cavity population when the pump is off,  $n_p \ll 10^{-2}$ , we need an on/off ratio much bigger than 80 dB. For that we combine the on/off ratio of the generator itself (isolation  $> 60$  dB) with a pin-diode pulse modulator gated by a square pulse (isolation  $> 60$  dB).
- Because the strong pump is usually applied a mechanical frequency away from the cavity, *i.e* only 90 cavity linewidth away from resonance, a lot of care was given to avoid non-negligible population at the cavity frequency. First the pump's amplitude and phase noise around  $\omega_c$  is filtered out using a home-made notch filter. For that we reflect the pump tone off of a critically coupled copper cavity (see Fig.S8). The filter is made from commercial copper tubing, has a quality factor of  $\kappa_{int} \approx \kappa_{ext} \approx 2$  MHz, and the attenuation of the notch filter exceed easily 50 dB. Second, by pulsing the microwave pump one broadens it in the frequency domain. Simply speaking, if the pump is turned *on* faster than the detuning with respect to the cavity  $\Delta_p = \pm\Omega_m$ , the cavity gets directly driven, producing unwanted population. To avoid this problem we chose a simple pulse shape with a Gaussian envelope given by the characteristic time  $\sigma = 200$  ns.
- From Eq.5, the pump power in the cavity feedline is close to  $0.5 \mu\text{W} = -33\text{dBm}$ . That high absolute power has two main consequences. First it cannot be dissipated at the mixing chamber stage: a  $-13\text{dBm}$  tone going through a 20 dB attenuator would dissipate almost  $50 \mu\text{W}$ , to be compared to the cooling power of the dilution unit, of the order of a few  $\mu\text{W}$  at base temperature. To avoid that issue we use a 20 dB directional coupler and route the transmitted signal back to the  $T = 4$  K stage to be dissipated in a  $50 \Omega$  load. Second, despite the high output power of the microwave generator (25 dBm), the attenuation of the coaxial line (from explicit attenuators and cable loss) had to be reduced to its bare minimum without any measurable thermal population of the cavity arising from 300 K radiation.

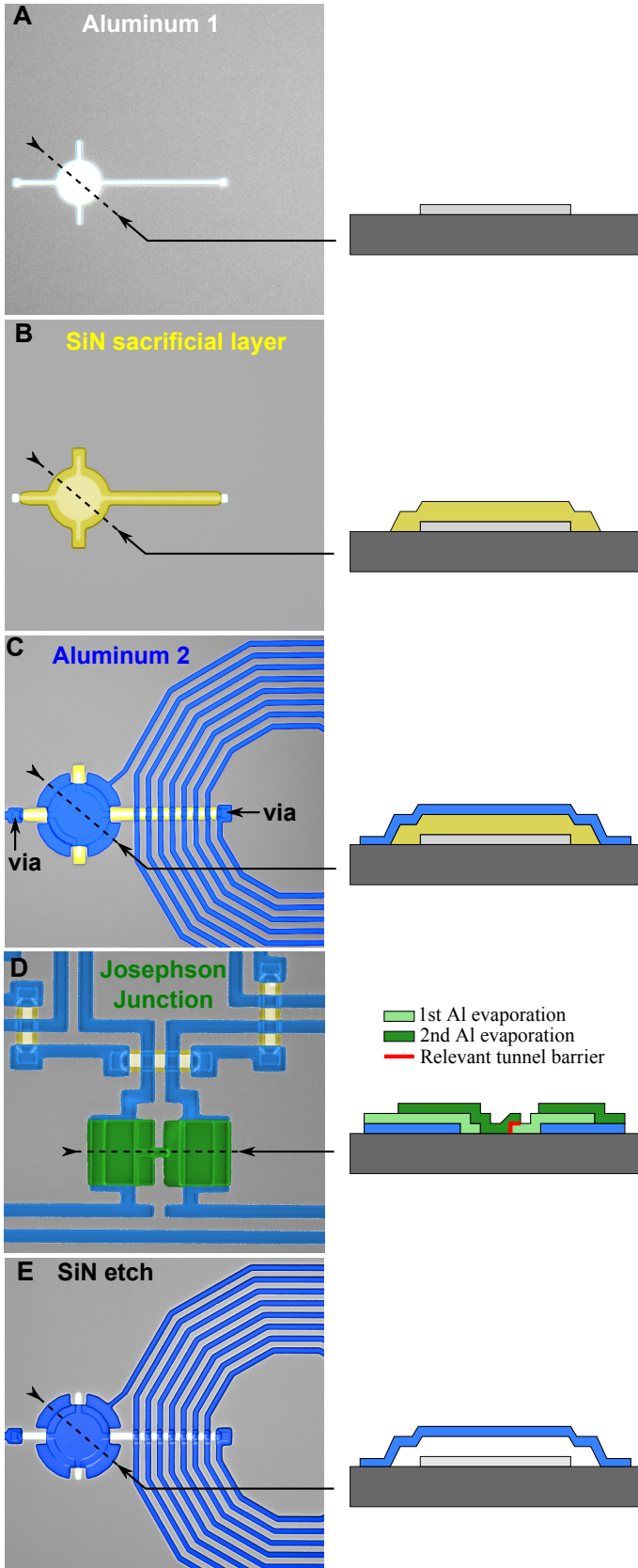


FIG. S6: **Device fabrication.** False-colored optical micrograph and side-view diagram at each step of the fabrication process. **(A)** We start by sputtering a 100 nm thick aluminum layer that is patterned by lithography and etched in a  $Cl_2/BCl_3$  plasma. This first layer forms the bottom plate of the cavity capacitor and the central wire of the cavity coil inductor, shown here in white. Also formed in this step are every short interconnection wires in the qubit and SQUID gradiometers (visible in **D**). **(B)** Next a sacrificial layer is deposited which will give rise to the vacuum gaps in the parallel plate capacitor and other crossovers, shown in yellow. This layer is a 200 nm thick  $SiN_x$  layer that is deposited by PECVD, patterned by lithography and etched in a  $CF_4/O_2$  plasma. **(C)** We sputter and pattern a second aluminum layer (100 nm thick, shown in blue), to define the top plate of the capacitor, the cavity coil, qubit coil and capacitor, and almost all the wiring. The electrical contact with the first aluminum layer, in the region not covered with  $SiN_x$ , is ensured by an in-situ argon plasma etch that removes the aluminum native oxide. **(D)** The Josephson junctions of the SQUID and the qubit (in green) are formed by a double angle aluminum evaporation separated by an in-situ oxidation<sup>13</sup>. Again, to ensure proper electrical contact with the previous aluminum layer we ion-mill the native oxide prior to the junction deposition. **(E)** Finally we release the mechanical membrane and the air bridges by etching the sacrificial layer away, in a high pressure, low power,  $SF_6$  plasma.

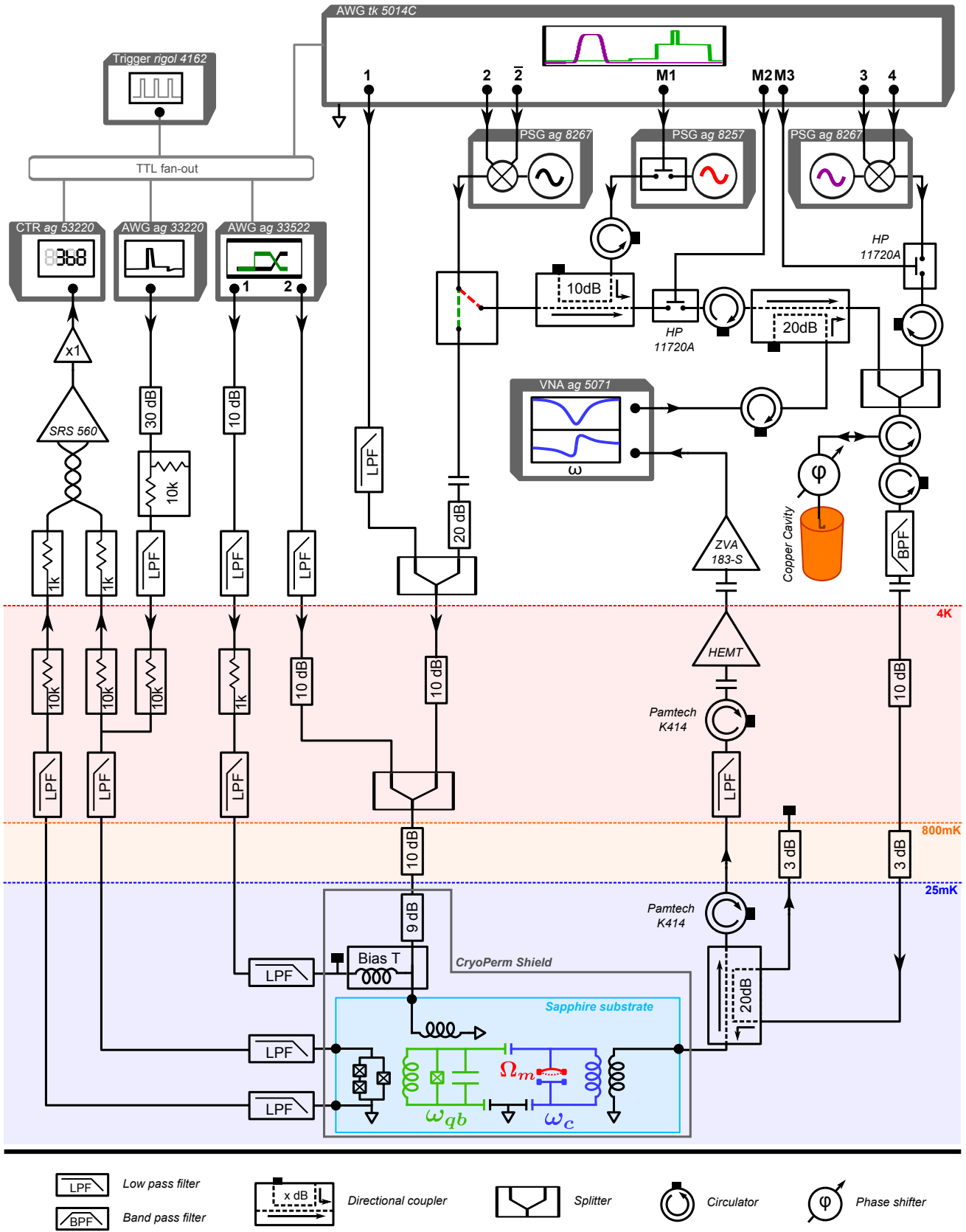


FIG. S7: Detailed experimental diagram

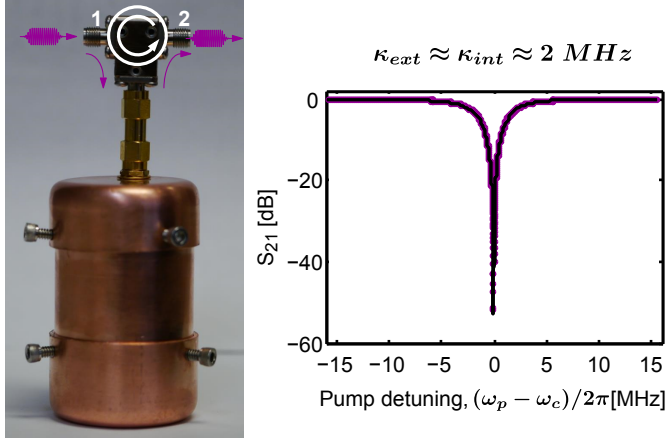


FIG. S8: **Copper cavity filter**. Left: picture of the cavity filter, connected to a circulator. Right: Transmitted power through the filter, tuned to resonate at the cavity frequency  $\omega_c$ .

We combine that main pump tone with two additional microwave drives, used to respectively pre-cool and displace the mechanical mode. The pre-cooling pulse is generated in a very similar way as the main pump and has a fixed frequency,  $\omega_{precool}$ , so that  $\Delta_{precool} = \omega_{precool} - \omega_c = -\Omega_m$ . To displace the mechanical mode we add another microwave pulse,  $\omega_{drive}$ , with  $\Delta_{drive} = \omega_{drive} - \omega_c = -2 * \Omega_m$ , that beats with the pre-cooling tone at the mechanical frequency, thus directly driving the mechanical mode.

Finally to measure the driven response of the cavity (Fig.2F) we use a Vector Network Analyser (VNA). A weak probe tone is added at room temperature, reflected off of the optomechanical device and amplified back up to room temperature. For these type of measurements the cavity filter is bypassed.

*Qubit control* The qubit is flux biased via an on-chip coil (mutual inductance  $\approx 2$  pH). The current through the coil comes from three distinct sources. The goal is to access a large range of flux (thus qubit frequency) with a large enough bandwidth, negligible dephasing and no excess dissipation at the mixing chamber stage of the dilution fridge.

- A very low frequency signal (Bandwidth  $\approx 2$  MHz) is generated at room-temperature with an AWG, then is attenuated and filtered at room temperature, before going through a 1 k $\Omega$  bias resistor at  $T = 4$  K. The signal is filtered, using commercial low-pass filters filled with lossy copper epoxy, at  $T = 4$  K (*VLFX-80*) and at base temperature (*VLFX-80+VLFX-650*). That very low frequency signal ensures a stable and non dissipative bias at  $\Phi = \Phi_0/2$  during the dcSQUID switching measurement and a bias at  $\Phi = 0$  otherwise.
- The two other signals (Bandwidth  $\approx 30$  MHz and  $\approx 200$  MHz) are generated at room temperature using AWGs, combined at  $T = 4$  K and routed down via unfiltered, attenuated, coaxial lines. The  $\approx 30$  MHz bias is used to move from  $\Phi = 0$ , where  $\omega_{qb}/2\pi \approx 13.5$  GHz, to a flux bias where  $\omega_{qb}/2\pi \approx 11$  GHz, about 800 MHz away from the cavity resonance. The high frequency bias is necessary for tuning the qubit in and out of resonance with the cavity faster than the coupling  $J = 12.5$  MHz. It is also necessary for the qubit tunneling measurement<sup>14</sup>.

The three signals are finally combined before the sample using of a custom bias-T that has a band-pass going down to dc on all three ports. For qubit state manipulation, microwave pulses are eventually added at room temperature to the high bandwidth bias signal using a diplexer (cross over frequency at 7.5 GHz).

*dcSQUID readout* The dcSQUID is current biased by use of a 10 k $\Omega$  bias resistor at  $T = 4$  K. The bias signal is generated at room temperature by an AWG, followed by a first step of filtering and attenuation. The signal is filtered again at  $T = 4$  K and at base temperature (same filters than qubit lines). The voltage that develops across the dcSQUID when it switches propagates through identically filtered lines up to room temperature where it is amplified and filtered by a low noise amplifier (*SRS-650*). The voltage goes through a unity-gain isolation amplifier and finally to a counter that records the number of switching events. A 5 KHz repetition rate ensures proper relaxation of the quasi-particles generated by the dcSQUID switching.

<sup>1</sup> S. Haroche, J. M. Raimond, *Exploring the Quantum: Atoms, Cavities, and Photons* (Oxford Univ. Press, 2006).

<sup>2</sup> J. R. Johansson, P. D. Nation, F. Nori, *Computer Physics Communications* **184**, 1234 (2013).

<sup>3</sup> J. D. Teufel, *et al.*, *Nature* **471**, 204 (2011).

<sup>4</sup> G. S. Agarwal, S. Huang, *Phys. Rev. A* **81**, 041803 (2010).

- <sup>5</sup> S. Weis, *et al.*, *Science* **330**, 1520 (2010).
- <sup>6</sup> A. A. Clerk, M. H. Devoret, S. M. Girvin, F. Marquardt, R. J. Schoelkopf, *Rev. Mod. Phys.* **82**, 1155 (2010).
- <sup>7</sup> J. D. Teufel, *et al.*, *Nature* **475**, 359 (2011).
- <sup>8</sup> T. A. Palomaki, J. D. Teufel, R. W. Simmonds, K. W. Lehnert, *Science* **342**, 710 (2013).
- <sup>9</sup> M. Aspelmeyer, T. J. Kippenberg, F. Marquardt, *ArXiv e-prints* **1303.0733** (2013).
- <sup>10</sup> J. W. Harlow, Microwave electromechanics: Measuring and manipulating the quantum state of a macroscopic mechanical oscillator, Ph.D. thesis, University of Colorado (2013).
- <sup>11</sup> J. S. Gao, J. Zmuidzinas, B. A. Mazin, H. G. LeDuc, P. K. Day, *Applied Physics Letters* **90**, 102507 (2007).
- <sup>12</sup> J. Gao, *et al.*, *Applied Physics Letters* **98**, 232508 (2011).
- <sup>13</sup> G. J. Dolan, *Applied Physics Letters* **31**, 337 (1977).
- <sup>14</sup> K. B. Cooper, *et al.*, *Physical Review Letters* **93**, 180401 (2004).